

# Detecting the relativistic bispectrum in 21cm intensity maps

Sheean Jolicoeur<sup>1</sup>, Roy Maartens<sup>1,2</sup>, Eline M. De Weerd<sup>3</sup>,  
Obinna Umeh<sup>2</sup>, Chris Clarkson<sup>3,1</sup>, Stefano Camera<sup>4,5,1</sup>

<sup>1</sup>Department of Physics & Astronomy, University of the Western Cape, Cape Town 7535, South Africa

<sup>2</sup>Institute of Cosmology & Gravitation, University of Portsmouth, Portsmouth PO1 3FX, UK

<sup>3</sup>School of Physics & Astronomy, Queen Mary University of London, London E1 4NS, UK

<sup>4</sup>Dipartimento di Fisica, Università degli Studi di Torino, 10125 Torino, Italy

<sup>5</sup>Istituto Nazionale di Fisica Nucleare, Sezione di Torino, 10125 Torino, Italy

E-mail: [jolicoeurshean@gmail.com](mailto:jolicoeurshean@gmail.com), [roy.maartens@gmail.com](mailto:roy.maartens@gmail.com),  
[e.deweerd@qmul.ac.uk](mailto:e.deweerd@qmul.ac.uk), [obinna.umeh@port.ac.uk](mailto:obinna.umeh@port.ac.uk), [chris.clarkson@qmul.ac.uk](mailto:chris.clarkson@qmul.ac.uk),  
[stefano.camera@unito.it](mailto:stefano.camera@unito.it)

**Abstract.** We investigate the detectability of leading-order relativistic effects in the bispectrum of future 21cm intensity mapping surveys. The relativistic signal arises from Doppler and other line-of-sight effects in redshift space. In the power spectrum of a single tracer, these effects are suppressed by a factor  $\mathcal{H}^2/k^2$ . By contrast, in the bispectrum the relativistic signal couples to short-scale modes, leading to an imaginary contribution that scales as  $\mathcal{H}/k$ , thus increasing the possibility of detection. Previous work has shown that this relativistic signal is detectable in a Stage IV H $\alpha$  galaxy survey. We show that the signal is also detectable by next-generation 21cm intensity maps, but typically with a lower signal-to-noise, due to foreground and telescope beam effects.

---

## Contents

<b>1</b>	<b>Introduction</b>	<b>1</b>
<b>2</b>	<b>Relativistic effects in the 21cm intensity bispectrum</b>	<b>2</b>
<b>3</b>	<b>Relativistic signal-to-noise ratio</b>	<b>5</b>
3.1	Nonlinearity	6
3.2	Effects of foregrounds	7
3.3	Maximum and minimum scales probed	8
3.4	Instrumental noise	9
3.5	Future HI intensity mapping surveys	10
<b>4</b>	<b>Forecasts for the relativistic signal-to-noise</b>	<b>12</b>
4.1	Single-dish mode	12
4.2	Interferometer mode	13
4.3	Reducing the radial foreground cut	14
<b>5</b>	<b>Conclusions</b>	<b>14</b>
<b>A</b>	<b>HI bias parameters</b>	<b>17</b>
<b>B</b>	<b>MeerKAT and SKA system temperatures</b>	<b>18</b>

---

## 1 Introduction

Next-generation galaxy surveys will allow for precision measurements of the bispectrum, bringing new information to improve constraints on cosmological parameters and to break some of their degeneracies (see e.g. [1–19]).

These surveys will typically probe very large volumes in the Universe, including ultra-large scales ( $k \lesssim k_{\text{eq}} \sim 0.01 \text{ Mpc}^{-1}$ ), which facilitates the detection of, or precision constraints on, primordial non-Gaussianity [20–25] and relativistic effects [26–35].

Redshift-space distortions (RSD) are the dominant observational effect on the number counts or brightness temperature at first and second order in perturbations. There are local relativistic corrections to standard RSD, arising from Doppler and other line-of-sight gradient terms, together with their couplings. In Fourier space, the leading-order corrections scale as  $i(\mathcal{H}/k)$ . In the tree-level power spectrum of a single tracer, the only nonzero contribution from these Doppler-type effects is from their square, since the power spectrum is necessarily real. As a result, the Doppler-type effects are further suppressed in the auto-power spectrum, scaling as  $(\mathcal{H}/k)^2$ .

The tree-level bispectrum of a single tracer is not forced to be real and it couples Doppler-type effects with the standard (‘Newtonian’) density + RSD term. Consequently, the leading-order relativistic contribution to the bispectrum scales as  $i(\mathcal{H}/k)$ . This means that the leading-order relativistic signal is more detectable in the bispectrum than the power spectrum, for a single tracer. In Fourier space, the dominant relativistic effect is a purely imaginary part of the bispectrum, as shown by [33, 34]. Our previous work [34] showed that it is detectable by a Stage IV spectroscopic galaxy survey.

In this work, we investigate the detectability of the relativistic signal in the bispectrum of various planned 21cm intensity mapping surveys at post-reionisation redshifts. The 21cm emission line of neutral hydrogen (HI) is measured without detecting the individual galaxies that contain HI. This results in brightness temperature maps that trace the large-scale structure with exquisite redshift precision. In Section 2 we discuss the leading order relativistic form of the temperature contrast up to second order, and its contribution to the bispectrum. Section 3 describes the signal, modelled using the tree-level bispectrum with the addition of a phenomenological model to account for RSD ‘fingers-of-god’ nonlinearity. Foreground contamination overwhelms the signal, and cleaning techniques must be applied which lead to a loss of signal in regions of Fourier space, which we take into account. We also discuss the effects of telescope beams and the instrumental noise. Our forecast signal-to-noise for future surveys is presented in Section 4, and we conclude in Section 5.

## 2 Relativistic effects in the 21cm intensity bispectrum

The HI brightness temperature measured at redshift  $z$  in direction  $\mathbf{n}$  is related to the observed number of 21cm emitters per redshift per solid angle,  $N_{\text{HI}}$ , as follows (see [36, 37] for details):

$$T_{\text{HI}}(z, \mathbf{n}) = \text{const.} \frac{N_{\text{HI}}(z, \mathbf{n})}{d_{\text{A}}(z, \mathbf{n})^2}, \quad (2.1)$$

where  $d_{\text{A}}$  is the angular diameter distance.

The background HI brightness temperature follows from (2.1) as [38]

$$\bar{T}_{\text{HI}}(z) = 189h \frac{(1+z)H_0}{\mathcal{H}(z)} \Omega_{\text{HI}}(z) \text{ mK}. \quad (2.2)$$

Here  $h = H_0/(100 \text{ km/s})$ ,  $\mathcal{H} = (\ln a)'$  is the conformal Hubble rate, and  $\Omega_{\text{HI}}(z)$  is the comoving HI density in units of the critical density today, which is currently poorly constrained by observations and is modelled by simulations. We use the fit in [39]:

$$\bar{T}_{\text{HI}}(z) = 0.056 + 0.23z - 0.024z^2 \text{ mK}. \quad (2.3)$$

The temperature fractional perturbation is

$$\Delta_{\text{HI}}(z, \mathbf{n}) = \frac{T_{\text{HI}}(z, \mathbf{n}) - \bar{T}_{\text{HI}}(z)}{\bar{T}_{\text{HI}}(z)}. \quad (2.4)$$

Using (2.1), this leads to the following perturbative expansion (our convention is  $X + X^{(2)}/2$ ). (A clear and concise derivation of the following expressions for  $\Delta$  and  $\Delta^{(2)}$  is given in Appendix A of [40].)

- **At first order** [36]:

$$\Delta \equiv \Delta_{\text{HI}}^{(1)} = \Delta_{\text{N}} + \Delta_{\text{D}}, \quad \Delta_{\text{N}} = b_1 \delta_{\text{m}} - \frac{1}{\mathcal{H}} \partial_r (\mathbf{v} \cdot \mathbf{n}), \quad \Delta_{\text{D}} = A (\mathbf{v} \cdot \mathbf{n}). \quad (2.5)$$

Here  $r$  is the radial comoving distance and  $\mathbf{v} = \nabla V$  is the peculiar velocity.  $\Delta_{\text{N}}$  is the standard density + RSD term, which scales as  $\delta_{\text{m}}$ .  $\Delta_{\text{D}}$  is the dominant relativistic correction, scaling as  $i(\mathcal{H}/k)\delta_{\text{m}}$  in Fourier space. This Doppler term has coefficient

$$A = b_e - 2 - \frac{\mathcal{H}'}{\mathcal{H}^2} = -\frac{d \ln [(1+z)\bar{T}_{\text{HI}}]}{d \ln(1+z)}, \quad (2.6)$$

where the evolution bias is [41]

$$b_e = -\frac{d \ln [(1+z)^{-1} \mathcal{H} \bar{T}_{\text{HI}}]}{d \ln(1+z)}. \quad (2.7)$$

We omit sub-leading relativistic corrections that scale as  $(\mathcal{H}/k)^2 \delta_m$ .

- **At second order** [34] (see also [33, 40, 42–44]):

$$\Delta^{(2)} \equiv \Delta_{\text{HI}}^{(2)} = \Delta_{\text{N}}^{(2)} + \Delta_{\text{D}}^{(2)}, \quad (2.8)$$

$$\Delta_{\text{N}}^{(2)} = b_1 \delta_m^{(2)} + b_2 (\delta_m)^2 + b_{s^2} s^2 + \text{RSD}^{(2)}, \quad (2.9)$$

$$\begin{aligned} \Delta_{\text{D}}^{(2)} = & A (\mathbf{v}^{(2)} \cdot \mathbf{n}) + 2 \left[ b_1 (A + f) + \frac{b'_1}{\mathcal{H}} \right] (\mathbf{v} \cdot \mathbf{n}) \delta_m + \frac{1}{\mathcal{H}} (8 - 4A - 3\Omega_m) (\mathbf{v} \cdot \mathbf{n}) \partial_r (\mathbf{v} \cdot \mathbf{n}) \\ & + \frac{2}{\mathcal{H}^2} [(\mathbf{v} \cdot \mathbf{n}) \partial_r^2 \Phi - \Phi \partial_r^2 (\mathbf{v} \cdot \mathbf{n})] - \frac{2}{\mathcal{H}} \partial_r (\mathbf{v} \cdot \mathbf{v}) + 2 \frac{b_1}{\mathcal{H}} \Phi \partial_r \delta_m. \end{aligned} \quad (2.10)$$

In (2.9),  $b_{s^2} s^2$  is the tidal bias contribution and  $\text{RSD}^{(2)}$  is the standard second-order RSD contribution (see [34] for details). The bias parameters are computed via a halo model (see Appendix A) and are shown in Figure 1, together with the evolution bias. In (2.10), we see the Doppler terms and the line-of-sight gradients that make up the dominant relativistic contribution.  $\Phi$  is the gravitational potential and  $\Omega_m = \Omega_{m0}(1+z)H_0^2/\mathcal{H}^2$ . We neglect sub-dominant relativistic effects in  $\Delta^{(2)}$  that scale as  $(\mathcal{H}/k)^2 (\delta_m)^2$ .

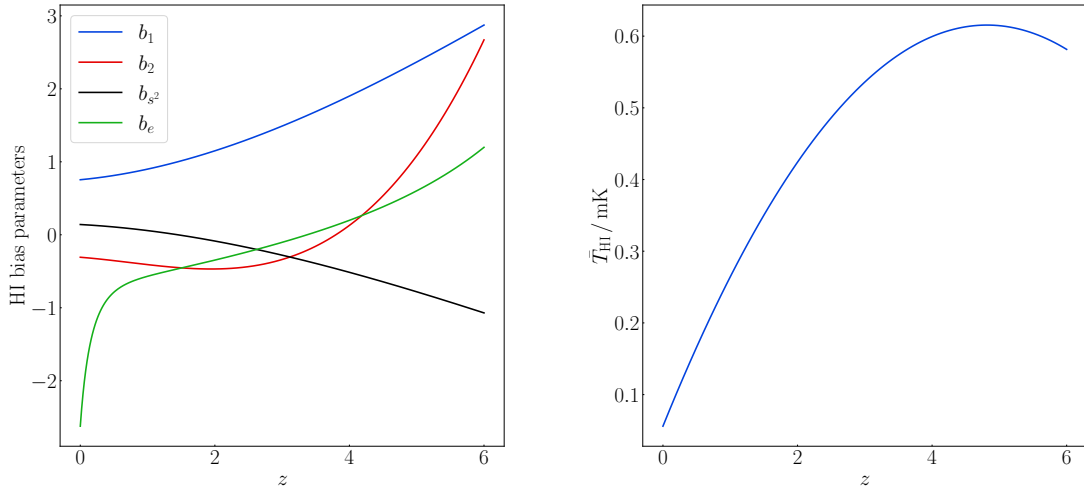


**Figure 1.** HI clustering and evolution bias parameters (left) and background temperature (right).

- **Lensing contribution:**

At first order, there is no lensing contribution to  $\Delta$  [36]. The general case of galaxy number density contrast contains a lensing contribution  $2(\mathcal{Q} - 1)\kappa$  to  $\Delta_g$ , where  $\kappa$  is the convergence [45]. For HI emitters in intensity mapping, the magnification bias satisfies

$$\mathcal{Q} \equiv -\frac{\partial \ln \bar{N}_{\text{HI}}}{\partial \ln L} \Big|_c = 1, \quad (2.11)$$

where  $c$  indicates evaluation at the luminosity cut.

At second order, (2.1) shows that there is also no contribution to  $\Delta^{(2)}$  from lensing convergence [43, 46]. We can recover this result from the full general expression for second-order number density contrast [47–51], by imposing (2.11) together with the conditions [43]

$$\left. \frac{\partial^2 \ln \bar{N}_{\text{HI}}}{\partial (\ln L)^2} \right|_c = 0, \quad \left. \frac{\partial b_1}{\partial \ln L} \right|_c = 0. \quad (2.12)$$

There remains however a lensing deflection contribution  $\nabla_{\perp a} \Delta \nabla_{\perp}^a \phi$  to  $\Delta^{(2)}$ , where  $\nabla_{\perp a}$  is a screen-space gradient and  $\phi$  is the lensing potential [42, 43, 46]. In the bispectrum the contribution of this term is negligible for equal-redshift correlations [18, 43]. Since we only consider the bispectrum at equal redshifts, we can safely neglect this term.

In Fourier space, the HI bispectrum at tree level is defined by

$$\langle \Delta(z, \mathbf{k}_1) \Delta(z, \mathbf{k}_2) \Delta^{(2)}(z, \mathbf{k}_3) \rangle + 2 \text{ cp} = 2(2\pi)^3 B_{\text{HI}}(z, \mathbf{k}_1, \mathbf{k}_2, \mathbf{k}_3) \delta^{\text{Dirac}}(\mathbf{k}_1 + \mathbf{k}_2 + \mathbf{k}_3), \quad (2.13)$$

where  $\text{cp}$  denotes cyclic permutation. It follows that

$$B_{\text{HI}}(z, \mathbf{k}_1, \mathbf{k}_2, \mathbf{k}_3) = \mathcal{K}^{(1)}(z, \mathbf{k}_1) \mathcal{K}^{(1)}(z, \mathbf{k}_2) \mathcal{K}^{(2)}(z, \mathbf{k}_1, \mathbf{k}_2, \mathbf{k}_3) P_{\text{m}}(z, k_1) P_{\text{m}}(z, k_2) + 2 \text{ cp}, \quad (2.14)$$

where  $P_{\text{m}}$  is the linear matter power spectrum (computed using CLASS [52]). From now on, we often drop the  $z$  dependence for brevity. The bispectrum kernels are as follows.

- **Standard (Newtonian) kernels:**

$$\mathcal{K}_{\text{N}}^{(1)}(\mathbf{k}_a) = b_1 + f \mu_a^2, \quad (2.15)$$

$$\mathcal{K}_{\text{N}}^{(2)}(\mathbf{k}_1, \mathbf{k}_2, \mathbf{k}_3) = b_1 F_2(\mathbf{k}_1, \mathbf{k}_2) + b_2 + f \mu_3^2 G_2(\mathbf{k}_1, \mathbf{k}_2) + f Z_2(\mathbf{k}_1, \mathbf{k}_2) + b_{s_2} S_2(\mathbf{k}_1, \mathbf{k}_2), \quad (2.16)$$

where  $f$  is the linear matter growth rate,  $\mu_a = \hat{\mathbf{k}}_a \cdot \mathbf{n}$  and the standard  $F_2, G_2, Z_2, S_2$  kernels are given in [34].

- **Leading-order relativistic kernels:**

$$\mathcal{K}_{\text{D}}^{(1)}(\mathbf{k}_a) = i \mathcal{H} f A \frac{\mu_a}{k_a}, \quad (2.17)$$

$$\begin{aligned} \mathcal{K}_{\text{D}}^{(2)}(\mathbf{k}_1, \mathbf{k}_2, \mathbf{k}_3) = i \mathcal{H} f \left\{ A \frac{\mu_3}{k_3} G_2(\mathbf{k}_1, \mathbf{k}_2) + \left[ b_1 (A + f) + \frac{b'_1}{\mathcal{H}} \right] \left( \frac{\mu_1}{k_1} + \frac{\mu_2}{k_2} \right) \right. \\ \left. - \frac{3}{2} \Omega_{\text{m}} \left( \mu_1^3 \frac{k_1}{k_2^2} + \mu_2^3 \frac{k_2}{k_1^2} \right) + \left[ \frac{3}{2} \Omega_{\text{m}} (1 + f) + 2f(A - 2) \right] \mu_1 \mu_2 \left( \frac{\mu_1}{k_2} + \frac{\mu_2}{k_1} \right) \right. \\ \left. + 2f \hat{\mathbf{k}}_1 \cdot \hat{\mathbf{k}}_2 \left( \frac{\mu_1}{k_1} + \frac{\mu_2}{k_2} \right) - \frac{3\Omega_{\text{m}} b_1}{2f} \left( \mu_1 \frac{k_1}{k_2^2} + \mu_2 \frac{k_2}{k_1^2} \right) \right\}, \quad (2.18) \end{aligned}$$

where  $A$  is given by (2.6). These follow from (2.5) and (2.10), and agree with [34] when we impose (2.6), (2.11) and (2.12).

- **Complex bispectrum:**

From (2.15)–(2.18) we see that  $B_{\text{HI}}$  is complex: the imaginary part is given purely by local relativistic corrections, while at leading order, i.e. neglecting relativistic terms of  $O(\mathcal{H}^2/k^2)$ , the real part is given purely by the standard Newtonian bispectrum:

$$\text{Re}(B_{\text{HI}}) = B_{\text{N}} = \mathcal{K}_{\text{N}}^{(1)}(\mathbf{k}_1)\mathcal{K}_{\text{N}}^{(1)}(\mathbf{k}_2)\mathcal{K}_{\text{N}}^{(2)}(\mathbf{k}_1, \mathbf{k}_2, \mathbf{k}_3)P_{\text{m}}(k_1)P_{\text{m}}(k_2) + 2 \text{ cp}, \quad (2.19)$$

$$\begin{aligned} \text{i Im}(B_{\text{HI}}) = B_{\text{D}} = & \left\{ \left[ \mathcal{K}_{\text{N}}^{(1)}(\mathbf{k}_1)\mathcal{K}_{\text{D}}^{(1)}(\mathbf{k}_2) + \mathcal{K}_{\text{D}}^{(1)}(\mathbf{k}_1)\mathcal{K}_{\text{N}}^{(1)}(\mathbf{k}_2) \right] \mathcal{K}_{\text{N}}^{(2)}(\mathbf{k}_1, \mathbf{k}_2, \mathbf{k}_3) \right. \\ & \left. + \mathcal{K}_{\text{N}}^{(1)}(\mathbf{k}_1)\mathcal{K}_{\text{N}}^{(1)}(\mathbf{k}_2)\mathcal{K}_{\text{D}}^{(2)}(\mathbf{k}_1, \mathbf{k}_2, \mathbf{k}_3) \right\} P_{\text{m}}(k_1)P_{\text{m}}(k_2) + 2 \text{ cp}. \end{aligned} \quad (2.20)$$

It is apparent that  $B_{\text{N}} \sim P_{\text{m}}^2$  while  $B_{\text{D}} \sim \text{i}(\mathcal{H}/k)P_{\text{m}}^2$ . Equation (2.20) makes explicit the coupling of relativistic and Newtonian terms in the bispectrum.

### 3 Relativistic signal-to-noise ratio

The signal-to-noise ratio for a bispectrum in the Gaussian case is given by  $\text{SNR}^2 = B^2/\text{Var}(B)$ , where the variance includes cosmic variance as well as noise. The relativistic part of the bispectrum at leading order is extracted as the imaginary part of the estimator for the bispectrum. For the variance, we use the fact that it is unaffected by relativistic corrections at leading order:  $\text{Var}(B_{\text{HI}}) = \text{Var}(B_{\text{N}}) + O(\mathcal{H}^2/k^2)$ , as shown in [34].

The bispectrum in each  $z$ -bin has 5 independent degrees of freedom, which we choose as the 3 sides  $k_a$  of the closed triangle and 2 angles ( $\theta_1 = \cos^{-1} \mu_1, \varphi$ ) that define the orientation of the triangle. The relativistic SNR per  $z$ -bin is then given by [34]

$$\text{SNR}(z)^2 = \sum_{k_a, \mu_1, \varphi} \frac{B_{\text{D}}(z, k_a, \mu_1, \varphi) B_{\text{D}}^*(z, k_a, \mu_1, \varphi)}{\text{Var}[B_{\text{N}}(z, k_a, \mu_1, \varphi)]}, \quad (3.1)$$

where we isolated the imaginary part, and the cumulative SNR is defined by

$$\text{SNR}(\leq z)^2 = \sum_{z'} \text{SNR}(z')^2. \quad (3.2)$$

The total SNR is  $\text{SNR}(\leq z_{\text{max}})$ .

The variance is estimated as

$$\text{Var}[B_{\text{N}}(z, k_a, \mu_1, \varphi)] = \frac{s_B \pi k_{\text{f}}(z)^3}{k_1 k_2 k_3 (\Delta k)^3} \frac{4\pi}{\Delta \mu_1 \Delta \varphi} \tilde{P}_{\text{HI}}(z, k_1, \mu_1) \tilde{P}_{\text{HI}}(z, k_2, \mu_2) \tilde{P}_{\text{HI}}(z, k_3, \mu_3). \quad (3.3)$$

Here

$$\tilde{P}_{\text{HI}}(z, k, \mu) = P_{\text{HI}}(z, k, \mu) + P_{\text{noise}}(z, k, \mu), \quad (3.4)$$

where the HI power spectrum is Newtonian at leading order:  $P_{\text{HI}} = P_{\text{N}} + O(\mathcal{H}^2/k^2)$ , with

$$P_{\text{N}}(z, k, \mu) = [b_1(z) + f(z)\mu^2]^2 P_{\text{m}}(z, k). \quad (3.5)$$

In (3.3), the multiplicity constant  $s_B = 6, 2, 1$  for equilateral, isosceles, and non-isosceles triangles, and  $\Delta k, \Delta \mu_1, \Delta \varphi$  are bin widths. We follow [23, 34] and choose the step lengths as

$$\Delta z = 0.1, \quad \Delta \mu = 0.04, \quad \Delta \varphi = \pi/25, \quad \Delta k(z) = k_{\text{f}}(z). \quad (3.6)$$

The fundamental mode  $k_f$  is an estimate of the minimum wavenumber included in the survey, and is determined in each redshift bin by the comoving volume of the bin centred at  $z$ :

$$k_f(z) = \frac{2\pi}{V(z)^{1/3}} \quad \text{with} \quad V(z) = \frac{4\pi}{3} f_{\text{sky}} [r(z + \Delta z/2)^3 - r(z - \Delta z/2)^3]. \quad (3.7)$$

Here  $f_{\text{sky}} = \Omega_{\text{sky}}/4\pi$  is the sky fraction covered by the survey.

### 3.1 Nonlinearity

The tree-level bispectrum is a perturbative model. In order to avoid scales where dark matter clustering becomes nonperturbative, we impose a maximum scale [34]

$$k_{\text{max}}(z) = 0.1h(1+z)^{2/(2+n_s)} \text{ Mpc}^{-1}. \quad (3.8)$$

However, applying this cut-off still includes nonperturbative RSD effects, i.e. the fingers-of-god damping. In order to take account of this, we follow [9, 23, 34] and use the following phenomenological model of the damping of redshift-space clustering due to nonlinear velocities:

$$P_{\text{HI}}(k, \mu, z) \rightarrow \exp\left[-\frac{1}{2}k^2\mu^2\sigma_P(z)^2\right] P_{\text{HI}}(k, \mu, z), \quad (3.9)$$

$$B_{\text{HI}}(k_a, \mu_a, z) \rightarrow \exp\left[-\frac{1}{2}(k_1^2\mu_1^2 + k_2^2\mu_2^2 + k_3^2\mu_3^2)\sigma_B(z)^2\right] B_{\text{HI}}(k_a, \mu_a, z). \quad (3.10)$$

Damping is effective for  $k \gtrsim \sqrt{2}/\sigma_P$  for the power spectrum and  $k \gtrsim \sqrt{2}/\sigma_B$  for the bispectrum. In this model, the damping parameters  $\sigma_P$  and  $\sigma_B$  are to be determined by data or simulations. We use a model for the power spectrum damping parameter based on HI simulations [53]:

$$\sigma_P(z) = 11h(1+z)^{-1.9} \exp\left[-(z/11)^2\right] h^{-1} \text{ Mpc}. \quad (3.11)$$

We are not aware of any simulation-based expression for  $\sigma_B$ , and we therefore take  $\sigma_B = \sigma_P$  as a first approximation. The effect of increasing  $\sigma_B$  is discussed in Section 5.

A further source of nonlinearity on weakly nonlinear scales that contributes to the bispectrum variance is the non-Gaussian effect due to mode coupling. We follow [23, 34] and take account of this using the simple model developed in [54], which modifies the variance as follows:

$$\text{Var}[B_{\text{N}}(\mathbf{k}_a)] \rightarrow \text{Var}[B_{\text{N}}(\mathbf{k}_a)] \left[1 + \frac{\delta\tilde{P}_{\text{N}}(\mathbf{k}_1)}{\tilde{P}_{\text{N}}(\mathbf{k}_1)} + \frac{\delta\tilde{P}_{\text{N}}(\mathbf{k}_2)}{\tilde{P}_{\text{N}}(\mathbf{k}_2)} + \frac{\delta\tilde{P}_{\text{N}}(\mathbf{k}_3)}{\tilde{P}_{\text{N}}(\mathbf{k}_3)}\right]. \quad (3.12)$$

Here the redshift dependence has been dropped for brevity, and

$$\delta\tilde{P}_{\text{N}}(\mathbf{k}) = \tilde{P}_{\text{N}}^{\text{nl}}(\mathbf{k}) - \tilde{P}_{\text{N}}(\mathbf{k}), \quad (3.13)$$

$$\tilde{P}_{\text{N}}^{\text{nl}}(\mathbf{k}) = (b_1 + f\mu^2)^2 P_{\text{m}}^{\text{nl}}(k) + P_{\text{noise}}(\mathbf{k}), \quad (3.14)$$

where  $\tilde{P}_{\text{N}} = P_{\text{N}} + P_{\text{noise}}$  and  $P_{\text{m}}^{\text{nl}}$  is the nonlinear matter power spectrum computed in CLASS with a modified Halofit emulator.

### 3.2 Effects of foregrounds

Foreground contamination is the major systematic confronting 21cm intensity mapping. Cleaning techniques are very efficient at recovering the cosmological signal in regions of  $(k_{\parallel}, k_{\perp})$  space (see e.g. [55–67]). A realistic model of bispectrum measurements should include modelling of foreground removal. However, our focus is on the relativistic signal in the bispectrum and so we take a simpler approach – by excising the regions of  $(k_{\parallel}, k_{\perp})$  space where foreground cleaning does not recover the signal efficiently.

HI intensity mapping surveys are planned for next-generation radio dish arrays, including MeerKAT<sup>1</sup>, SKA1-MID<sup>2</sup> and HIRAX<sup>3</sup>. We will also consider surveys with PUMA<sup>4</sup> in its initial phase (Petite) (note that PUMA is currently still a proposal). Intensity mapping surveys can be done in 2 survey modes:

- Single-dish (SD) mode: auto-correlation signals from single dishes are added.
- Interferometer (IF) mode: cross-correlation signals from array elements are combined.

In both SD- and IF-mode surveys, foreground cleaning effectively removes large-scale radial modes because of the smoothness in frequency of the main foreground emissions. In order to model the effects of foreground cleaning, we remove radial modes  $k_{\parallel} \equiv \mu k$  that are smaller than a critical scale  $k_{\parallel\text{fg}}$  [23]. We impose this via an exponential damping factor [56]:

$$D_{\text{fg}}(k, \mu) = 1 - \exp \left[ - \left( \frac{\mu k}{k_{\parallel\text{fg}}} \right)^2 \right] \quad \text{for SD and IF survey modes.} \quad (3.15)$$

Then

$$P_{\text{HI}}(k, \mu, z) \rightarrow D_{\text{fg}}(k, \mu) P_{\text{HI}}(k, \mu, z), \quad (3.16)$$

$$B_{\text{HI}}(k_a, \mu_a, z) \rightarrow D_{\text{fg}}(k_1, \mu_1) D_{\text{fg}}(k_2, \mu_2) D_{\text{fg}}(k_3, \mu_3) B_{\text{HI}}(k_a, \mu_a, z). \quad (3.17)$$

The value of  $k_{\parallel\text{fg}}$  can be reduced by techniques which reconstruct long modes from the information in measured short modes. This technique has been applied to HI intensity mapping by [68, 69]. Taking into account reconstruction, we choose

$$k_{\parallel\text{fg}} = 0.01 h \text{ Mpc}^{-1}, \quad (3.18)$$

but we will also consider an optimistic case,  $k_{\parallel\text{fg}} = 0.005 h \text{ Mpc}^{-1}$ , that anticipates further developments of the reconstruction technique.

IF-mode surveys lose additional signal due to the fact that interferometers are chromatic, i.e., a fixed physical baseline length probes different angular scales at different frequencies. This causes smooth foregrounds to leak into high- $k_{\perp}$  modes [62, 63, 70]. The signal loss may be accounted for by excluding the region known as the foreground wedge [55, 58]:

$$|k_{\parallel}| > k_{\text{wedge}}(z) k_{\perp} \quad \text{for IF survey mode,} \quad (3.19)$$

where  $k_{\perp} = \sqrt{1 - \mu^2} k$  and  $k_{\text{wedge}}$  is modelled as

$$k_{\text{wedge}}(z) = r(z) \mathcal{H}(z) \sin [0.61 N_w \theta_b(z)]. \quad (3.20)$$

<sup>1</sup>[www.sarao.ac.za/science/meerkat/](http://www.sarao.ac.za/science/meerkat/)

<sup>2</sup>[www.skatelescope.org/](http://www.skatelescope.org/)

<sup>3</sup>[hirax.ukzn.ac.za/](http://hirax.ukzn.ac.za/)

<sup>4</sup>[www.puma.bnl.gov/](http://www.puma.bnl.gov/)



The beam (defining the IF field of view) is given for a dish array by

$$\theta_b(z) = 1.22 \frac{\lambda(z)}{D_d}, \quad (3.21)$$

where  $\lambda(z) = \lambda_{21}(1+z)$  and  $D_d$  is the dish diameter.  $N_w$  is the number of primary beams away from the beam centre that contaminate the signal. The wedge effect is a technical problem that can be mitigated (and in principle removed) by calibration of baselines [71]. Following [24], we take

$$N_w = 0, 1, 3, \quad (3.22)$$

where 0 is the most optimistic possibility (wedge removed by calibration) and 3 is a pessimistic case.

### 3.3 Maximum and minimum scales probed

The nonlinearity limit  $k \leq k_{\max}(z)$  given in (3.8), defines a minimum wavelength  $2\pi/k_{\max}(z)$  that is independent of surveys and is determined purely by dark matter clustering. It applies to both SD- and IF-mode surveys. However, in the case of IF-mode surveys, there is also a lower limit on angular scales, i.e. an upper limit on transverse wavenumbers, via  $k_{\perp} = 2\pi/(r\theta)$ . This arises because the maximum baseline  $D_{\max}$  determines the angular resolution and the upper limit can be roughly estimated by a cut-off [18, 24, 56, 70]

$$k_{\perp}^{\text{IF}}(z) \approx \frac{2\pi D_{\max}}{r(z)\lambda(z)}. \quad (3.23)$$

In our computations, we do not use this cut-off since it is effectively imposed by the baseline density factor (see Section 3.4).

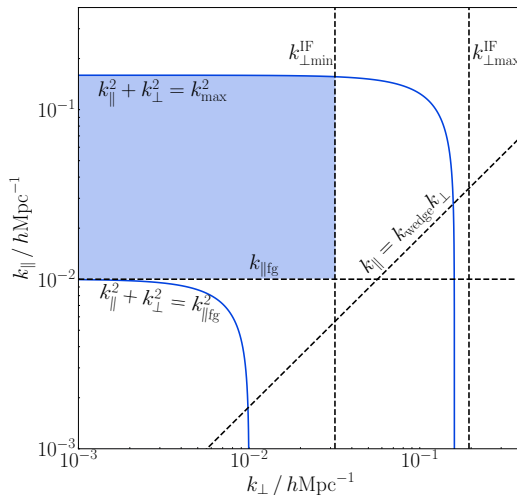


**Figure 2.** Schematic of important scales in the  $k_{\parallel}, k_{\perp}$ -plane at fixed  $z$ . Shading indicates the included region for SD mode (light) and IF mode (dark).

In principle, the maximum wavelength probed by HI intensity surveys at redshift  $z$  is  $2\pi/k_f(z)$ , where the fundamental mode  $k_f$  is determined by the comoving volume of the

redshift bin, via (3.7). However, foreground cleaning imposes on both SD- and IF-mode surveys the limiting minimum radial wavenumber  $k_{\parallel\text{fg}}$ , given by (3.18). Since  $k^2 = k_{\parallel}^2 + k_{\perp}^2$ , this means that

$$k > k_{\parallel\text{fg}} \quad \text{which implies} \quad k > k_{\min} = \max\{k_{\text{f}}(z), k_{\parallel\text{fg}}\}. \quad (3.24)$$

In IF-mode surveys there is a further minimum wavenumber, corresponding to the maximum angular scale that can be probed. This limit depends on the minimum baseline and is given by [18, 24, 56, 70]:

$$k_{\perp\text{min}}^{\text{IF}}(z) = \frac{2\pi}{r(z)\theta_{\text{b}}(z)}. \quad (3.25)$$

Since  $k > k_{\perp}$ , we have

$$k > k_{\min} = \max\{k_{\perp\text{min}}^{\text{IF}}(z), k_{\text{f}}(z), k_{\parallel\text{fg}}\} \quad \text{for IF surveys.} \quad (3.26)$$

The scales from foreground cleaning and the maximum and minimum scales are shown schematically in Figure 2. This does not include the effects of the beam in SD mode; see Figure 5 below.

### 3.4 Instrumental noise

In HI intensity mapping for the scales and redshifts we consider, the shot noise is much smaller than the instrumental noise for next-generation surveys<sup>5</sup> and can be safely neglected [38, 73]. The noise power spectrum for the fractional temperature perturbation is then determined by instrumental noise and is given by [56, 70].<sup>6</sup>

$$P_{\text{noise}}(z) = \frac{2\pi f_{\text{sky}}}{\nu_{21} t_{\text{tot}}} \frac{(1+z)r(z)^2}{\mathcal{H}(z)} \left[ \frac{T_{\text{sys}}(z)}{\bar{T}_{\text{HI}}(z)} \right]^2 \frac{\alpha(z, k_{\perp})}{\beta(z, k_{\perp})^2} h^{-3} \text{Mpc}^3. \quad (3.27)$$

Here  $t_{\text{tot}}$  is the total observing time, and the system temperature may be modelled as [63]:

$$T_{\text{sys}}(z) = T_{\text{d}}(z) + T_{\text{sky}}(z) = T_{\text{d}}(z) + 2.7 + 25 \left[ \frac{400 \text{ MHz}}{\nu_{21}} (1+z) \right]^{2.75} \text{K}, \quad (3.28)$$

where  $T_{\text{d}}$  is the dish receiver temperature. (We consider only dish arrays.)

In (3.27), the dish density factor  $\alpha$  and the effective beam  $\beta$  depend on the survey mode, as follows [18, 56, 62, 63, 75]:

$$\alpha_{\text{SD}} = \frac{1}{N_{\text{d}}}, \quad \beta_{\text{SD}} = \exp \left[ -\frac{k_{\perp}^2 r(z)^2 \theta_{\text{b}}(z)^2}{16 \ln 2} \right], \quad (3.29)$$

$$\alpha_{\text{IF}} = \left[ \frac{\lambda(z)^2}{A_{\text{e}}} \right]^2 \frac{1}{n_{\text{b}}(z, k_{\perp})}, \quad \beta_{\text{IF}} = \theta_{\text{b}}(z). \quad (3.30)$$

Here  $N_{\text{d}}$  is the number of dishes and  $A_{\text{e}}$  is the effective beam area:

$$A_{\text{e}} = 0.7 A_{\text{d}}, \quad A_{\text{d}} = \frac{\pi}{4} D_{\text{d}}^2. \quad (3.31)$$

<sup>5</sup>For the futuristic PUMA (Full) survey, the noise is low enough to be comparable to the shot noise [72].

<sup>6</sup>It is also possible to put the beam factor  $\beta$  in the signal, rather than in the noise; see e.g. [74] for a discussion.

The dimensionless  $n_b$  is the baseline density in the image plane (assuming azimuthal symmetry), which is determined by the array distribution. The total number of baselines is  $\int d^2\mathbf{u} n_b(u) = N_d(N_d - 1)/2$ . A physical baseline length  $L$  is related to an image-plane scale  $u$  as

$$L = u\lambda = \frac{k_\perp r}{2\pi} \lambda. \quad (3.32)$$

Then the image-plane and physical distributions of the array are related by [63]

$$n_b(z, u) = \lambda(z)^2 n_b^{\text{phys}}(L). \quad (3.33)$$

### 3.5 Future HI intensity mapping surveys

We consider surveys proposed for the following dish arrays:

- SD mode: MeerKAT, SKA1-MID.
- IF mode: HIRAX, PUMA (Petite).

The survey specifications are given in Table 1, based on [24, 39, 65, 76, 77]. Limiting wavenumbers for large wavelengths are shown for these surveys in Figure 3: the fundamental wavenumber (3.7), the minimum radial wavenumber (3.18) from foreground cleaning and the IF-mode minimum wavenumber (3.25).

**Table 1.** HI intensity mapping survey specifications. (For \*, see Appendix B.)

Survey	Redshift range	$f_{\text{sky}}$	$t_{\text{tot}}$ [ $10^3$ hr]	$T_d$ [K]	$D_d$ [m]	$N_d$	$D_{\text{max}}$ [m]
MeerKAT L Band	0.10–0.58	0.10	4	*	13.5	64	–
MeerKAT UHF Band	0.40–1.45	0.10	4	*	13.5	64	–
SKA1-MID Band 1	0.35–3.05	0.48	10	*	15.0	197	–
SKA1-MID Band 2	0.10–0.49	0.48	10	*	15.0	197	–
HIRAX	0.75–2.00	0.36	10	50	6.0	1024	270
PUMA (Petite)	2.00–6.00	0.50	40	50	6.0	5000	600

**Table 2.** Parameters in (3.34) (from [63]).

Survey	$a$	$b$	$c$	$d$	$e$	$N_s$
HIRAX	0.4847	−0.3300	1.3157	1.5974	6.8390	32
PUMA (Petite)	0.5698	−0.5274	0.8358	1.6635	7.3177	100

For the system temperature, we use the results of measurements and simulations for MeerKAT and SKA1-MID, given in Appendix B. For HIRAX and PUMA, we use the fit (3.28).

In IF mode, HIRAX is assumed to be a square-packed array, while PUMA is taken as hexagonal-packed in a circular area, with 50% fill factor. We follow [24] and use the fitting formula from [63] for the baseline density of such arrays:

$$n_b^{\text{phys}}(L) = \left(\frac{N_s}{D_d}\right)^2 \frac{a + b(L/L_s)}{1 + c(L/L_s)^d} \exp[-(L/L_s)^e], \quad (3.34)$$

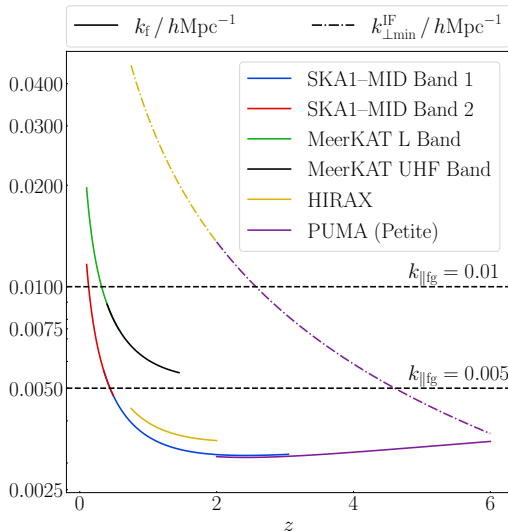


**Figure 3.** Minimum wavenumbers for the surveys, where  $k$  is subject to (3.24) (SD) or (3.26) (IF).

where  $L_s = N_s D_d$  and  $N_s^2 = N_d$ . The parameters in (3.34) are given in Table 2, and  $n_b^{\text{phys}}(L)$  is shown in Figure 4.

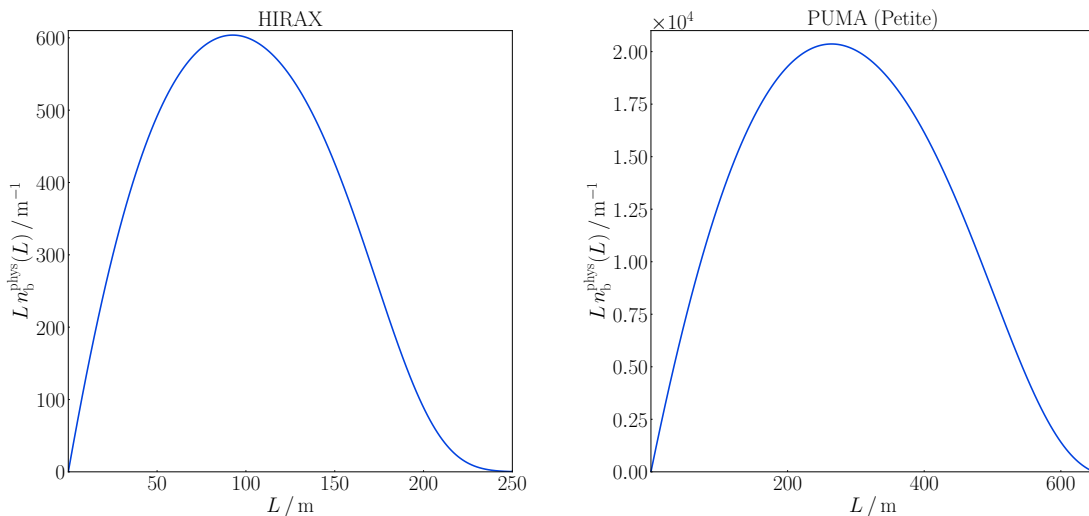


**Figure 4.** Physical baseline density models for HIRAX (left) and PUMA (right).

In the case of PUMA, we take account of the 50% fill factor as follows. We use double the number of dishes to define  $N_s$  for the computation of (3.34), i.e.  $N_s^2 = 2 \times 5000$ . Then we remove half of the dishes without changing the baseline, i.e. without changing the shape and ground-area of the array.

The noise power spectra of the surveys at fixed redshift are displayed in Figure 5. For SD-mode surveys, the poor angular resolution is reflected in the blow-up of noise due to the beam in (3.29). The minimum transverse scale for IF-mode surveys is shown as a sharp

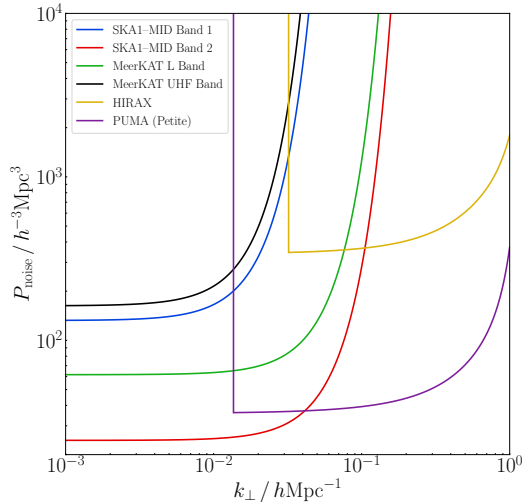


**Figure 5.** Noise power spectra of the SD-mode surveys (at  $z = 0.4$  for low- $z_{\max}$  bands and  $z = 1$  for high- $z_{\max}$  bands) and IF-mode surveys (HIRAX at  $z = 1$ , PUMA at  $z = 2$ ).

cut-off, as in (3.25), with effectively infinite noise. Figure 5 also shows the smooth blow-up of IF-mode noise on small transverse scales, which results from the fact that  $n_b \rightarrow 0$  as the baseline approaches its maximum  $D_{\max}$  (see Figure 4). The unbounded increase of noise kills the signal, corresponding to the approximate cut-off scale (3.23).

## 4 Forecasts for the relativistic signal-to-noise

### 4.1 Single-dish mode

The SNR of the relativistic part of the bispectrum is shown in Figure 6, per  $z$ -bin and cumulative.

**Table 3.** Total SNR for single-dish mode surveys.

Survey	Total SNR
MeerKAT UHF Band	2.5
MeerKAT L Band	1.8
MeerKAT L+UHF Bands	<b>3.0</b>
SKA1-MID Band 1	5.8
SKA1-MID Band 2	3.0
SKA1-MID Bands 1+2	<b>6.6</b>

The total SNR for the HI IM surveys in SD mode is  $3 \lesssim \text{SNR} \lesssim 7$ , with the high- $z_{\max}$  bands giving higher SNR. Table 3 displays the predicted total SNR for the SD-mode HI IM surveys. We can slightly improve the best total SNR by combining measurements in the two bands, for both MeerKAT and SKA. In general, since we ignore cross-redshift correlations, we can sum in quadrature the per-bin values,  $\text{SNR}(z_i)$ , as if they were a collection of bins from the same set of observations. However, it must be noted that the two bands overlap in the redshift range  $0.40 \leq z \leq 0.58$  for MeerKAT and  $0.35 \leq z \leq 0.49$  for SKA. In that range,

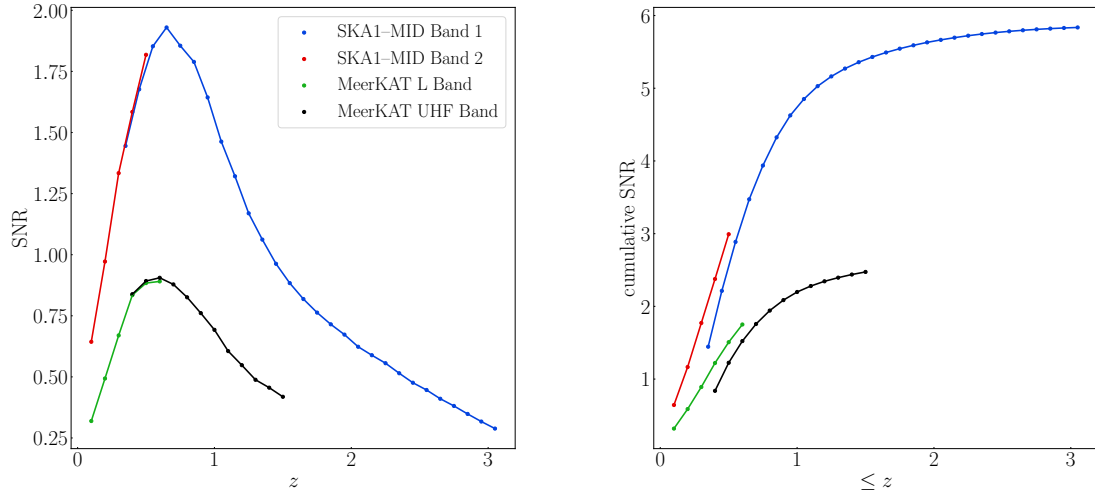


**Figure 6.** SNR of the relativistic bispectrum per  $z$ -bin (*left*) and cumulative (*right*) for SD-mode surveys.

we follow a conservative approach and only consider the band yielding the largest value of SNR. The values obtained are shown in Table 3.

The best case, SKA1 Bands 1+2, gives a total SNR  $\sim 6$  that is detectable, a few times smaller than the SNR predicted for a Stage IV  $H\alpha$  (similar to *Euclid*) spectroscopic survey [34].

## 4.2 Interferometer mode

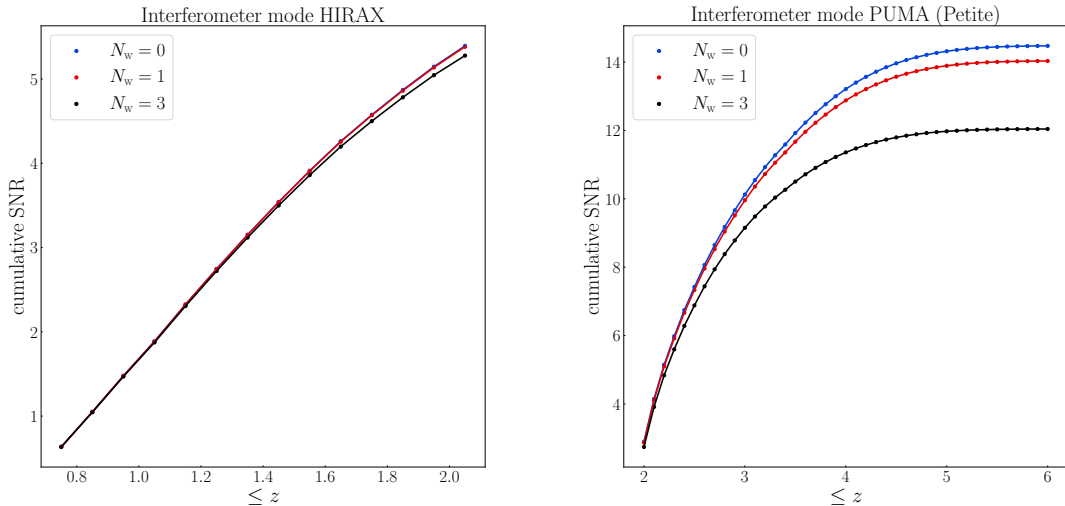


**Figure 7.** Cumulative SNR of the relativistic bispectrum for IF-mode surveys.

Figure 7 shows the forecasts of the relativistic bispectrum SNR for HIRAX and PUMA, using three values of the wedge parameter  $N_w$ . HIRAX predicts SNR values slightly lower than an SKA SD-mode survey. The proposed PUMA survey (the ‘Petite’ or PUMA–5K phase of the full or PUMA–32K proposal) gives the highest SNR, at a level similar to a Stage IV H $\alpha$  (*Euclid*-like) spectroscopic survey. This SNR would safely detect the relativistic signal. Note that PUMA is more sensitive than HIRAX to the  $N_w$  parameter. Table 4 gives the predicted total SNR for the IF-mode surveys.

**Table 4.** Total SNR for interferometer-mode surveys.

Survey \ $N_w$	0	1	3
HIRAX	5.4	<b>5.4</b>	5.3
PUMA (Petite)	14.5	<b>14.0</b>	12.0

### 4.3 Reducing the radial foreground cut

We investigate how much improvement in SNR results if we increase the number of very large scale modes by reducing the radial foreground cut to  $k_{\parallel\text{fg}} = 0.005 \text{ hMpc}^{-1}$ . Such a reduction may be achieved by future advances in reconstruction techniques.

It turns out that the SNR is relatively insensitive to this reduction in  $k_{\parallel\text{fg}}$ : very little gain in SNR is achieved, as shown in Tables 5 and 6.

**Table 5.** Total SNR for single-dish mode surveys with  $k_{\parallel\text{fg}} = 0.005 \text{ hMpc}^{-1}$ .

Survey	Total SNR
MeerKAT UHF Band	2.8
MeerKAT L Band	2.0
MeerKAT L+UHF Bands	<b>3.4</b>
SKA1-MID Band 1	6.5
SKA1-MID Band 2	3.4
SKA1-MID Bands 1+2	<b>7.3</b>

**Table 6.** Total SNR for interferometer-mode surveys with  $k_{\parallel\text{fg}} = 0.005 \text{ hMpc}^{-1}$ .

Survey \ $N_w$	0	1	3
HIRAX	5.6	<b>5.6</b>	5.5
PUMA (Petite)	15.2	<b>14.6</b>	12.5

## 5 Conclusions

The imaginary part of the galaxy bispectrum at leading order is a unique signal that is purely relativistic [33] – and that can be readily extracted from the full bispectrum. In Fourier space, the leading-order local lightcone effects that generate the Doppler-type signal scale

as  $i(\mathcal{H}/k)$  (see (2.17) and (2.18)). In the galaxy power spectrum for a single tracer, these Doppler-type contributions only occur squared, thus scaling as  $\mathcal{H}^2/k^2$ . Only a cross-power spectrum analysis of two different tracers will generate an imaginary contribution [78]. For single tracers, the relativistic Doppler-type signal in the power spectrum is therefore highly suppressed and not detectable, even for a cosmic-variance limited survey [37].

However, in the bispectrum of a single tracer, the  $i(\mathcal{H}/k)$  relativistic signal survives because it couples with the Newtonian terms [33]. This increases the chance of detectability and, as shown by [34], the SNR forecast for a Stage IV H $\alpha$  galaxy spectroscopic survey (similar to *Euclid*) is  $\sim 17$ .

We extended the analysis of [34] to HI intensity mapping spectroscopic surveys, which requires significant additions in order to deal with foreground contamination and the complexities of instrumental noise (that dominates over shot noise). As expected, loss of signal due to foreground cleaning and telescope beam effects reduces the SNR for the next-generation surveys on MeerKAT, SKA1-MID and HIRAX. We forecast a detectable SNR  $\sim 6$  for SKA1 and  $\sim 5$  for HIRAX. The proposed PUMA survey in its Petite or 5,000-dish first phase (before the futuristic full survey with 32,000 dishes) delivers a SNR  $\sim 14$ , comparable to that of a Stage IV H $\alpha$  galaxy survey.

Surveys in single-dish mode (MeerKAT, SKA1) suffer from poor angular resolution so that the Newtonian short-scale transverse modes are suppressed. On the other hand, the interferometer-mode surveys (HIRAX, PUMA) do not probe ultra-large scales as well as SD-mode surveys because the maximum length scale is determined by the minimum baseline (3.25), as shown in Figure 5.

We investigated the effect of a more optimistic radial wavenumber cut and found that the improvement in SNR is small. This means that detection of the relativistic signal in the bispectrum does not require scales with  $k \lesssim 0.01h/\text{Mpc}$ .

There are some caveats to our results and pointers for future work:

- In common with nearly all work on the Fourier-space bispectrum that includes RSD, we implicitly make a flat-sky assumption, based on the fixed global direction  $\mathbf{n}$ . This is an issue when probing ultra-large scales – which applies not only to our case but also to all work on constraining primordial non-Gaussianity via the Fourier bispectrum. The flat-sky analysis loses accuracy as  $\theta$  increases, where  $\theta$  is the maximum opening angle to the three-point correlations at the given redshift. The corresponding comoving transverse scale is  $k_{\perp}(z) = 2\pi/[r(z)\theta]$ . There is a threshold scale  $\theta_{\text{fs}}$ , beyond which the approximation fails – i.e., for  $\theta > \theta_{\text{fs}}$ , or equivalently,  $k_{\perp} < k_{\perp\text{fs}}$ , the SNR is not reliable.

For IF-mode surveys, the flat-sky assumption is reasonable if  $\theta_{\text{fs}} > \theta_{\text{b}}$ , where  $\theta_{\text{b}}$  is the beam, given by (3.21). If we estimate that  $\theta_{\text{fs}} \sim 10^\circ$  (see [79]), then this condition holds for HIRAX, and for PUMA up to redshift 3 (see Figure 3). Consequently, the flat-sky assumption is reasonable for HIRAX. However for PUMA at  $z > 3$  and for the SD-mode surveys, there are modes with  $k_{\perp} < k_{\perp\text{fs}}$  and the accuracy of the SNR will be affected for these modes.

Including wide-angle effects is a key target for future work that constrains relativistic effects or primordial non-Gaussianity via the bispectrum. In fact, this is also important for standard cosmological constraints. Corrections to the global flat-sky analysis of the Fourier bispectrum can be made by using a local flat-sky approximation [1, 6]. Such corrections are typically approximate and do not incorporate the full wide-angle effect. Ultimately, one needs to use the full-sky 3-point correlation function or the



full-sky angular bispectrum (see e.g. [11, 18, 26, 28]) to properly include all wide-angle correlations. These alternatives are computationally much more intensive than the Fourier analysis.

- Also in common with other work on the Fourier power spectrum and bispectrum, we neglect cross-correlations among redshift bins. This is justified by the exquisite redshift accuracy of HI intensity mapping, allowing for sharp-edged redshift bins, which in turn implies small or no overlap between them. Integrated effects will in principle induce correlations along the line-of-sight direction, but this is not going to be relevant in our case since the dominant integrated contribution is weak lensing magnification, which vanishes in HI intensity mapping [36, 37, 43, 46]. Ultimately, only approximate solutions are possible in Fourier space and a complete treatment would require the angular bispectrum or 3-point correlation function.
- In the absence of a simulation-based model for the bispectrum RSD damping parameter  $\sigma_B$ , we set it equal to the power spectrum damping parameter  $\sigma_P$ , for which we used a fit from simulations given in [53]. Realistically, we expect that  $\sigma_B > \sigma_P$ . We tested the impact on the SNR of increasing  $\sigma_B$  to  $\sigma_B = 1.5 \sigma_P$  and found that it leads to only a small decrease in SNR.

## Acknowledgements

We thank Emanuele Castorina and Dionysis Karagiannis for helpful comments. SJ and RM are supported by the South African Radio Astronomy Observatory (SARAO) and the National Research Foundation (Grant No. 75415). RM and OU are supported by the UK Science & Technology Facilities Council (STFC) Consolidated Grant ST/S000550/1. CC is supported by STFC Consolidated Grant ST/P000592/1. SC acknowledges the support from the Ministero degli Affari Esteri della Cooperazione Internazionale - Direzione Generale per la Promozione del Sistema Paese Progetto di Grande Rilevanza ZA18GR02. SC is funded by MIUR through the Rita Levi Montalcini project ‘PROMETHEUS – Probing and Relating Observables with Multi-wavelength Experiments to Help Enlightening the Universe’s Structure’.

## A HI bias parameters

We follow [42] to compute  $b_1$  and  $b_2$  from a halo-model approach:

$$b_1 = 1 + \left\langle \frac{2p + (q\nu - 1)[1 + (q\nu)^p]}{\delta_{\text{cr}}[1 + (q\nu)^p]} \right\rangle_{\text{m}}, \quad (\text{A.1})$$

$$b_2 = \frac{8}{21}(b_1 - 1) + \left\langle \frac{2p(2p + 2\nu q - 1) + q\nu(q\nu - 3)[1 + (q\nu)^p]}{\delta_{\text{cr}}^2[1 + (q\nu)^p]} \right\rangle_{\text{m}}, \quad (\text{A.2})$$

where the parameters  $p$ ,  $q$  and  $\nu$  are related to the Sheth-Tormen distribution function (see [80–82] for more details), and  $\delta_{\text{cr}}$  is the critical density at which halos collapse spherically [83],

$$\delta_{\text{c}}(z) = \frac{3(12\pi)^{2/3}}{20} [1 + 0.0123 \log \Omega_{\text{m}}(z)]. \quad (\text{A.3})$$

The mass average is defined by

$$\langle X_h(z, \mathbf{x}) \rangle_{\text{m}} = \frac{\int_{M_-}^{M_+} dM X_h(z, \mathbf{x}, M) M_{\text{HI}}(M) n_h(z, \mathbf{x}, M)}{\int_{M_-}^{M_+} dM M_{\text{HI}}(M) n_h(z, \mathbf{x}, M)}, \quad (\text{A.4})$$

where  $M$  is the mass of halos that can host HI gas, and  $M_{\pm}$  are the lower and upper mass limits, which are related to the circular velocities of the galaxies [56].  $n_h$  is the halo mass function [20, 80, 81], and  $M_{\text{HI}}$  is the HI mass function, which is assumed to follow a power law [60],

$$M_{\text{HI}}(M) \propto M^{0.6}. \quad (\text{A.5})$$

Figure 1 shows the numerical results from (A.1) and (A.2). Fitting formulas for the bias parameters are

$$b_1(z) = 0.754 + 0.0877z + 0.0607z^2 - 0.00274z^3, \quad (\text{A.6})$$

$$b_2(z) = -0.308 - 0.0724z - 0.0534z^2 + 0.0247z^3. \quad (\text{A.7})$$

Assuming that halo formation is a local process in Lagrangian space and that there is no initial tidal bias, the tidal bias is [20]:

$$b_{s^2} = \frac{4}{7}(1 - b_1). \quad (\text{A.8})$$

## B MeerKAT and SKA system temperatures

**Table 7.** System temperatures for MeerKAT and SKA1-MID, used in Figure 8 (from [84]).

MeerKAT L Band		MeerKAT UHF Band		SKA1-MID Band 1		SKA1-MID Band 2	
$z$	$T_{\text{sys}} / \text{K}$	$z$	$T_{\text{sys}} / \text{K}$	$z$	$T_{\text{sys}} / \text{K}$	$z$	$T_{\text{sys}} / \text{K}$
0.136	19.2	0.420	20.3	0.403	27.2	0.115	16.4
0.183	19.7	0.495	21.0	0.470	26.9	0.168	16.6
0.235	20.3	0.578	21.7	0.539	26.8	0.223	16.8
0.291	20.9	0.671	22.5	0.612	26.9	0.280	17.0
0.352	21.5	0.775	23.5	0.767	27.5	0.341	17.2
0.420	22.3	0.893	24.7	0.850	28.1	0.403	17.6
0.495	23.1	1.03	26.1	0.938	28.8	0.470	18.0
0.578	24.0	1.18	27.9	1.03	29.8		
		1.37	30.3	1.12	30.8		
		1.45	31.5	1.22	32.1		
				1.33	33.5		
				1.44	35.2		
				1.55	37.1		
				1.67	39.2		
				1.80	41.6		
				1.93	44.2		
				2.07	47.2		
				2.22	50.6		
				2.37	54.4		
				2.54	58.6		
				2.69	63.4		
				2.87	68.8		
				3.05	74.8		

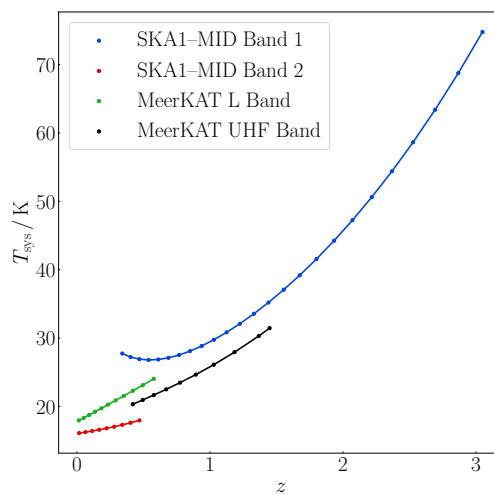


**Figure 8.**  $T_{\text{sys}}$  for the different frequency bands of MeerKAT and SKA1 (from Table 7).

## References

- [1] R. Scoccimarro, *Fast Estimators for Redshift-Space Clustering*, *Phys. Rev.* **D92** (2015), no. 8 083532, [[arXiv:1506.02729](#)].
- [2] M. Tellarini, A. J. Ross, G. Tasinato, and D. Wands, *Galaxy bispectrum, primordial non-Gaussianity and redshift space distortions*, *JCAP* **1606** (2016), no. 06 014, [[arXiv:1603.06814](#)].
- [3] H. Gil-Marín, W. J. Percival, L. Verde, J. R. Brownstein, C.-H. Chuang, F.-S. Kitaura, S. A. Rodríguez-Torres, and M. D. Olmstead, *The clustering of galaxies in the SDSS-III Baryon Oscillation Spectroscopic Survey: RSD measurement from the power spectrum and bispectrum of the DR12 BOSS galaxies*, *Mon. Not. Roy. Astron. Soc.* **465** (2017), no. 2 1757–1788, [[arXiv:1606.00439](#)].
- [4] Z. Slepian et al., *Detection of baryon acoustic oscillation features in the large-scale three-point correlation function of SDSS BOSS DR12 CMASS galaxies*, *Mon. Not. Roy. Astron. Soc.* **469** (2017), no. 2 1738–1751, [[arXiv:1607.06097](#)].
- [5] P. Gagrani and L. Samushia, *Information Content of the Angular Multipoles of Redshift-Space Galaxy Bispectrum*, *Mon. Not. Roy. Astron. Soc.* **467** (2017), no. 1 928–935, [[arXiv:1610.03488](#)].
- [6] N. S. Sugiyama, S. Saito, F. Beutler, and H.-J. Seo, *A complete FFT-based decomposition formalism for the redshift-space bispectrum*, *Mon. Not. Roy. Astron. Soc.* **484** (2019), no. 1 364–384, [[arXiv:1803.02132](#)].
- [7] V. Desjacques, D. Jeong, and F. Schmidt, *The Galaxy Power Spectrum and Bispectrum in Redshift Space*, *JCAP* **12** (2018) 035, [[arXiv:1806.04015](#)].
- [8] H. L. Child, M. Takada, T. Nishimichi, T. Sunayama, Z. Slepian, S. Habib, and K. Heitmann, *Bispectrum as Baryon Acoustic Oscillation Interferometer*, *Phys. Rev. D* **98** (2018), no. 12 123521, [[arXiv:1806.11147](#)].
- [9] V. Yankelevich and C. Porciani, *Cosmological information in the redshift-space bispectrum*, *Mon. Not. Roy. Astron. Soc.* **483** (2019), no. 2 2078–2099, [[arXiv:1807.07076](#)].
- [10] C. J. Schmit, A. F. Heavens, and J. R. Pritchard, *The gravitational and lensing-ISW bispectrum of 21 cm radiation*, *Mon. Not. Roy. Astron. Soc.* **483** (2019), no. 3 4259–4275, [[arXiv:1810.00973](#)].
- [11] E. Di Dio, R. Durrer, R. Maartens, F. Montanari, and O. Umeh, *The Full-Sky Angular Bispectrum in Redshift Space*, *JCAP* **04** (2019) 053, [[arXiv:1812.09297](#)].
- [12] D. Gualdi, H. Gil-Marín, M. Manera, B. Joachimi, and O. Lahav, *Geometrical compression: a new method to enhance the BOSS galaxy bispectrum monopole constraints*, *Mon. Not. Roy. Astron. Soc.* **484** (2019), no. 1 L29–L34, [[arXiv:1901.00987](#)].
- [13] D. Sarkar, S. Majumdar, and S. Bharadwaj, *Modelling the post-reionization neutral hydrogen (HI) 21-cm bispectrum*, *Mon. Not. Roy. Astron. Soc.* **490** (2019), no. 2 2880–2889, [[arXiv:1907.01819](#)].
- [14] A. Chudaykin and M. M. Ivanov, *Measuring neutrino masses with large-scale structure: Euclid forecast with controlled theoretical error*, *JCAP* **11** (2019) 034, [[arXiv:1907.06666](#)].
- [15] A. Oddo, E. Sefusatti, C. Porciani, P. Monaco, and A. G. Sánchez, *Toward a robust inference method for the galaxy bispectrum: likelihood function and model selection*, *JCAP* **03** (2020) 056, [[arXiv:1908.01774](#)].
- [16] N. S. Sugiyama, S. Saito, F. Beutler, and H.-J. Seo, *Perturbation theory approach to predict the covariance matrices of the galaxy power spectrum and bispectrum in redshift space*, *Mon. Not. Roy. Astron. Soc.* **497** (2020), no. 2 1684, [[arXiv:1908.06234](#)].

- [17] O. H. Philcox and D. J. Eisenstein, *Computing the Small-Scale Galaxy Power Spectrum and Bispectrum in Configuration-Space*, *Mon. Not. Roy. Astron. Soc.* **492** (2020), no. 1 1214–1242, [[arXiv:1912.01010](#)].
- [18] R. Durrer, M. Jalilvand, R. Kothari, R. Maartens, and F. Montanari, *Full-sky bispectrum in redshift space for 21cm intensity maps*, *JCAP* **12** (2020) 003, [[arXiv:2008.02266](#)].
- [19] F. Montanari and S. Camera, *Speeding up the detectability of the harmonic-space galaxy bispectrum*, *JCAP* **01** (2021) 002, [[arXiv:2008.11131](#)].
- [20] M. Tellarini, A. J. Ross, G. Tasinato, and D. Wands, *Non-local bias in the halo bispectrum with primordial non-Gaussianity*, *JCAP* **1507** (2015), no. 07 004, [[arXiv:1504.00324](#)].
- [21] C. A. Watkinson, S. Majumdar, J. R. Pritchard, and R. Mondal, *A fast estimator for the bispectrum and beyond: a practical method for measuring non-Gaussianity in 21-cm maps*, *Mon. Not. Roy. Astron. Soc.* **472** (2017), no. 2 2436–2446, [[arXiv:1705.06284](#)].
- [22] S. Majumdar, J. R. Pritchard, R. Mondal, C. A. Watkinson, S. Bharadwaj, and G. Mellema, *Quantifying the non-Gaussianity in the EoR 21-cm signal through bispectrum*, *Mon. Not. Roy. Astron. Soc.* **476** (2018), no. 3 4007–4024, [[arXiv:1708.08458](#)].
- [23] D. Karagiannis, A. Lazanu, M. Liguori, A. Raccanelli, N. Bartolo, and L. Verde, *Constraining primordial non-Gaussianity with bispectrum and power spectrum from upcoming optical and radio surveys*, *Mon. Not. Roy. Astron. Soc.* **478** (2018), no. 1 1341–1376, [[arXiv:1801.09280](#)].
- [24] D. Karagiannis, A. Slosar, and M. Liguori, *Forecasts on Primordial non-Gaussianity from 21 cm Intensity Mapping experiments*, *JCAP* **11** (2020) 052, [[arXiv:1911.03964](#)].
- [25] S. Bharadwaj, A. Mazumdar, and D. Sarkar, *Quantifying the Redshift Space Distortion of the Bispectrum I: Primordial Non-Gaussianity*, *Mon. Not. Roy. Astron. Soc.* **493** (2020), no. 1 594–602, [[arXiv:2001.10243](#)].
- [26] A. Kehagias, A. M. Dizgah, J. Noreña, H. Perrier, and A. Riotto, *A Consistency Relation for the Observed Galaxy Bispectrum and the Local non-Gaussianity from Relativistic Corrections*, *JCAP* **1508** (2015), no. 08 018, [[arXiv:1503.04467](#)].
- [27] O. Umeh, S. Jolicoeur, R. Maartens, and C. Clarkson, *A general relativistic signature in the galaxy bispectrum: the local effects of observing on the lightcone*, *JCAP* **1703** (2017) 003, [[arXiv:1610.03351](#)].
- [28] E. Di Dio, H. Perrier, R. Durrer, G. Marozzi, A. M. Dizgah, J. Noreña, and A. Riotto, *Non-Gaussianities due to Relativistic Corrections to the Observed Galaxy Bispectrum*, *JCAP* **1703** (2017), no. 03 006, [[arXiv:1611.03720](#)].
- [29] S. Jolicoeur, O. Umeh, R. Maartens, and C. Clarkson, *Imprints of local lightcone projection effects on the galaxy bispectrum. II*, *JCAP* **1709** (2017) 040, [[arXiv:1703.09630](#)].
- [30] D. Bertacca, A. Raccanelli, N. Bartolo, M. Liguori, S. Matarrese, and L. Verde, *Relativistic wide-angle galaxy bispectrum on the light-cone*, *Phys. Rev. D* **97** (2018), no. 2 023531, [[arXiv:1705.09306](#)].
- [31] S. Jolicoeur, O. Umeh, R. Maartens, and C. Clarkson, *Imprints of local lightcone projection effects on the galaxy bispectrum. Part III. Relativistic corrections from nonlinear dynamical evolution on large-scales*, *JCAP* **1803** (2018), no. 03 036, [[arXiv:1711.01812](#)].
- [32] K. Koyama, O. Umeh, R. Maartens, and D. Bertacca, *The observed galaxy bispectrum from single-field inflation in the squeezed limit*, *JCAP* **07** (2018) 050, [[arXiv:1805.09189](#)].
- [33] C. Clarkson, E. M. de Weerd, S. Jolicoeur, R. Maartens, and O. Umeh, *The dipole of the galaxy bispectrum*, *Mon. Not. Roy. Astron. Soc.* **486** (2019), no. 1 L101–L104, [[arXiv:1812.09512](#)].
- [34] R. Maartens, S. Jolicoeur, O. Umeh, E. M. De Weerd, C. Clarkson, and S. Camera, *Detecting the relativistic galaxy bispectrum*, *JCAP* **03** (2020), no. 03 065, [[arXiv:1911.02398](#)].

- [35] D. Jeong and F. Schmidt, *Parity-odd galaxy bispectrum*, *Phys. Rev. D* **102** (2020), no. 2 023530, [[arXiv:1906.05198](#)].
- [36] A. Hall, C. Bonvin, and A. Challinor, *Testing General Relativity with 21-cm intensity mapping*, *Phys. Rev. D* **87** (2013), no. 6 064026, [[arXiv:1212.0728](#)].
- [37] D. Alonso, P. Bull, P. G. Ferreira, R. Maartens, and M. Santos, *Ultra large-scale cosmology in next-generation experiments with single tracers*, *Astrophys. J.* **814** (2015), no. 2 145, [[arXiv:1505.07596](#)].
- [38] F. Villaescusa-Navarro et al., *Ingredients for 21 cm Intensity Mapping*, *Astrophys. J.* **866** (2018), no. 2 135, [[arXiv:1804.09180](#)].
- [39] MeerKLASS Collaboration, M. G. Santos et al., *MeerKLASS: MeerKAT Large Area Synoptic Survey*, in *MeerKAT Science: On the Pathway to the SKA*, 9, 2017. [[arXiv:1709.06099](#)].
- [40] E. Di Dio and U. Seljak, *The relativistic dipole and gravitational redshift on LSS*, *JCAP* **04** (2019) 050, [[arXiv:1811.03054](#)].
- [41] J. Fonseca, S. Camera, M. Santos, and R. Maartens, *Hunting down horizon-scale effects with multi-wavelength surveys*, *Astrophys. J.* **812** (2015), no. 2 L22, [[arXiv:1507.04605](#)].
- [42] O. Umeh, R. Maartens, and M. Santos, *Nonlinear modulation of the HI power spectrum on ultra-large scales. I*, *JCAP* **1603** (2016), no. 03 061, [[arXiv:1509.03786](#)].
- [43] E. Di Dio, R. Durrer, G. Marozzi, and F. Montanari, *The bispectrum of relativistic galaxy number counts*, *JCAP* **1601** (2016) 016, [[arXiv:1510.04202](#)].
- [44] O. Umeh, *Imprint of non-linear effects on HI intensity mapping on large scales*, *JCAP* **1706** (2017), no. 06 005, [[arXiv:1611.04963](#)].
- [45] A. Challinor and A. Lewis, *The linear power spectrum of observed source number counts*, *Phys. Rev.* **D84** (2011) 043516, [[arXiv:1105.5292](#)].
- [46] M. Jalilvand, E. Majerotto, R. Durrer, and M. Kunz, *Intensity mapping of the 21 cm emission: lensing*, *JCAP* **1901** (2019), no. 01 020, [[arXiv:1807.01351](#)].
- [47] D. Bertacca, R. Maartens, and C. Clarkson, *Observed galaxy number counts on the lightcone up to second order: I. Main result*, *JCAP* **1409** (2014), no. 09 037, [[arXiv:1405.4403](#)].
- [48] D. Bertacca, R. Maartens, and C. Clarkson, *Observed galaxy number counts on the lightcone up to second order: II. Derivation*, *JCAP* **1411** (2014), no. 11 013, [[arXiv:1406.0319](#)].
- [49] J. Yoo and M. Zaldarriaga, *Beyond the Linear-Order Relativistic Effect in Galaxy Clustering: Second-Order Gauge-Invariant Formalism*, *Phys. Rev.* **D90** (2014), no. 2 023513, [[arXiv:1406.4140](#)].
- [50] E. Di Dio, R. Durrer, G. Marozzi, and F. Montanari, *Galaxy number counts to second order and their bispectrum*, *JCAP* **1412** (2014) 017, [[arXiv:1407.0376](#)]. [Erratum: JCAP 1506 (2015) E01].
- [51] D. Bertacca, *Observed galaxy number counts on the light cone up to second order: III. Magnification bias*, *Class. Quant. Grav.* **32** (2015), no. 19 195011, [[arXiv:1409.2024](#)].
- [52] D. Blas, J. Lesgourgues, and T. Tram, *The Cosmic Linear Anisotropy Solving System (CLASS) II: Approximation schemes*, *JCAP* **1107** (2011) 034, [[arXiv:1104.2933](#)].
- [53] D. Sarkar and S. Bharadwaj, *Redshift-space distortions of the HI 21-cm intensity mapping signal due to the internal motions within galaxies*, *Mon. Not. Roy. Astron. Soc.* **487** (2019), no. 4 5666–5678, [[arXiv:1906.07032](#)].
- [54] K. C. Chan and L. Blot, *Assessment of the Information Content of the Power Spectrum and Bispectrum*, *Phys. Rev.* **D96** (2017), no. 2 023528, [[arXiv:1610.06585](#)].



- [55] J. C. Pober et al., *What Next-Generation 21 cm Power Spectrum Measurements Can Teach Us About the Epoch of Reionization*, *Astrophys. J.* **782** (2014) 66, [[arXiv:1310.7031](#)].
- [56] P. Bull, P. G. Ferreira, P. Patel, and M. G. Santos, *Late-time cosmology with 21cm intensity mapping experiments*, *Astrophys. J.* **803** (2015), no. 1 21, [[arXiv:1405.1452](#)].
- [57] D. Alonso, P. Bull, P. G. Ferreira, and M. G. Santos, *Blind foreground subtraction for intensity mapping experiments*, *Mon. Not. Roy. Astron. Soc.* **447** (2015) 400, [[arXiv:1409.8667](#)].
- [58] J. C. Pober, *The Impact of Foregrounds on Redshift Space Distortion Measurements With the Highly-Redshifted 21 cm Line*, *Mon. Not. Roy. Astron. Soc.* **447** (2015), no. 2 1705–1712, [[arXiv:1411.2050](#)].
- [59] L. Wolz, F. B. Abdalla, D. Alonso, C. Blake, P. Bull, T.-C. Chang, P. G. Ferreira, C.-Y. Kuo, M. G. Santos, and R. Shaw, *Foreground Subtraction in Intensity Mapping with the SKA*, *PoS AASKA14* (2015) 035, [[arXiv:1501.03823](#)].
- [60] M. G. Santos et al., *Cosmology from a SKA HI intensity mapping survey*, *PoS AASKA14* (2015) 019, [[arXiv:1501.03989](#)].
- [61] J. Shaw, K. Sigurdson, M. Sitwell, A. Stebbins, and U.-L. Pen, *Coaxing cosmic 21 cm fluctuations from the polarized sky using m-mode analysis*, *Phys. Rev. D* **91** (2015), no. 8 083514, [[arXiv:1401.2095](#)].
- [62] A. Obuljen, E. Castorina, F. Villaescusa-Navarro, and M. Viel, *High-redshift post-reionization cosmology with 21cm intensity mapping*, *JCAP* **05** (2018) 004, [[arXiv:1709.07893](#)].
- [63] **Cosmic Visions 21 cm** Collaboration, R. Ansari et al., *Inflation and Early Dark Energy with a Stage II Hydrogen Intensity Mapping experiment*, [[arXiv:1810.09572](#)].
- [64] A. Witzemann, D. Alonso, J. Fonseca, and M. G. Santos, *Simulated multitracer analyses with HI intensity mapping*, *Mon. Not. Roy. Astron. Soc.* **485** (2019), no. 4 5519–5531, [[arXiv:1808.03093](#)].
- [65] **Square Kilometre Array Cosmology Science Working Group** Collaboration, D. J. Bacon et al., *Cosmology with Phase 1 of the Square Kilometre Array; Red Book 2018: Technical specifications and performance forecasts*, [[arXiv:1811.02743](#)].
- [66] J. Asorey, D. Parkinson, F. Shi, Y.-S. Song, K. Ahn, J. Kim, J. Yao, L. Zhang, and S. Zuo, *HIR4: cosmology from a simulated neutral hydrogen full sky using Horizon Run 4*, *Mon. Not. Roy. Astron. Soc.* **495** (2020), no. 2 1788–1806, [[arXiv:2001.00833](#)].
- [67] S. Cunnington, A. Pourtsidou, P. S. Soares, C. Blake, and D. Bacon, *Multipole expansion for HI intensity mapping experiments: simulations and modelling*, *Mon. Not. Roy. Astron. Soc.* **496** (2020), no. 1 415–433, [[arXiv:2002.05626](#)].
- [68] H.-M. Zhu, U.-L. Pen, Y. Yu, and X. Chen, *Recovering lost 21 cm radial modes via cosmic tidal reconstruction*, *Phys. Rev. D* **98** (2018), no. 4 043511, [[arXiv:1610.07062](#)].
- [69] C. Modi, M. White, A. Slosar, and E. Castorina, *Reconstructing large-scale structure with neutral hydrogen surveys*, *JCAP* **11** (2019) 023, [[arXiv:1907.02330](#)].
- [70] D. Alonso, P. G. Ferreira, M. J. Jarvis, and K. Moodley, *Calibrating photometric redshifts with intensity mapping observations*, *Phys. Rev. D* **96** (2017), no. 4 043515, [[arXiv:1704.01941](#)].
- [71] A. Ghosh, F. Mertens, and L. V. E. Koopmans, *Deconvolving the wedge: maximum-likelihood power spectra via spherical-wave visibility modelling*, *Mon. Not. Roy. Astron. Soc.* **474** (2018), no. 4 4552–4563, [[arXiv:1709.06752](#)].
- [72] S.-F. Chen, E. Castorina, M. White, and A. Slosar, *Synergies between radio, optical and microwave observations at high redshift*, *JCAP* **07** (2019) 023, [[arXiv:1810.00911](#)].

- [73] E. Castorina and F. Villaescusa-Navarro, *On the spatial distribution of neutral hydrogen in the Universe: bias and shot-noise of the HI power spectrum*, *Mon. Not. Roy. Astron. Soc.* **471** (2017), no. 2 1788–1796, [[arXiv:1609.05157](#)].
- [74] J. L. Bernal, P. C. Breyse, H. Gil-Marín, and E. D. Kovetz, *User’s guide to extracting cosmological information from line-intensity maps*, *Phys. Rev. D* **100** (2019), no. 12 123522, [[arXiv:1907.10067](#)].
- [75] M. Jalilvand, E. Majerotto, C. Bonvin, F. Lacasa, M. Kunz, W. Naidoo, and K. Moodley, *New Estimator for Gravitational Lensing Using Galaxy and Intensity Mapping Surveys*, *Phys. Rev. Lett.* **124** (2020), no. 3 031101, [[arXiv:1907.00071](#)].
- [76] PUMA Collaboration, A. Slosar et al., *Packed Ultra-wideband Mapping Array (PUMA): A Radio Telescope for Cosmology and Transients*, [arXiv:1907.12559](#).
- [77] E. Castorina et al., *Packed Ultra-wideband Mapping Array (PUMA): Astro2020 RFI Response*, [arXiv:2002.05072](#).
- [78] P. McDonald, *Gravitational redshift and other redshift-space distortions of the imaginary part of the power spectrum*, *JCAP* **0911** (2009) 026, [[arXiv:0907.5220](#)].
- [79] T. Matsubara, *The Correlation function in redshift space: General formula with wide angle effects and cosmological distortions*, *Astrophys. J.* **535** (2000) 1, [[astro-ph/9908056](#)].
- [80] R. K. Sheth, H. J. Mo, and G. Tormen, *Ellipsoidal collapse and an improved model for the number and spatial distribution of dark matter haloes*, *Mon. Not. Roy. Astron. Soc.* **323** (2001) 1, [[astro-ph/9907024](#)].
- [81] R. K. Sheth and G. Tormen, *An Excursion set model of hierarchical clustering : Ellipsoidal collapse and the moving barrier*, *Mon. Not. Roy. Astron. Soc.* **329** (2002) 61, [[astro-ph/0105113](#)].
- [82] R. K. Sheth and G. Tormen, *Large scale bias and the peak background split*, *Mon. Not. Roy. Astron. Soc.* **308** (1999) 119, [[astro-ph/9901122](#)].
- [83] T. Kitayama and Y. Suto, *Semianalytical predictions for statistical properties of x-ray clusters of galaxies in cold dark matter universes*, *Astrophys. J.* **469** (1996) 480, [[astro-ph/9604141](#)].
- [84] J. Fonseca, J.-A. Viljoen, and R. Maartens, *Constraints on the growth rate using the observed galaxy power spectrum*, *JCAP* **1912** (2019), no. 12 028, [[arXiv:1907.02975](#)].